

THE TOPOLOGY AND SIZE OF THE UNIVERSE FROM THE COSMIC MICROWAVE BACKGROUND

GRIGOR ASLANYAN AND ANEESH V. MANOHAR

Department of Physics, University of California at San Diego, La Jolla, CA 92093

ABSTRACT

We study the possibility that the universe has compact topologies \mathbb{T}^3 , $\mathbb{T}^2 \times \mathbb{R}^1$, or $S^1 \times \mathbb{R}^2$ using the seven-year WMAP data. The maximum likelihood 95% confidence intervals for the size L of the compact direction are $1.7 \leq L/L_0 \leq 2.1$, $1.8 \leq L/L_0 \leq 2.0$, $1.2 \leq L/L_0 \leq 2.1$ for the three cases, respectively, where $L_0 = 14.4$ Gpc is the distance to the last scattering surface. An infinite universe is compatible with the data at 4.3σ . We find using a Bayesian analysis that the most probable universe has topology $\mathbb{T}^2 \times \mathbb{R}^1$, with $L/L_0 = 1.9$.

Subject headings:

1. INTRODUCTION

General relativity is a local theory and does not predict or constrain the global properties of the spacetime manifold describing our universe, which have to be constrained through observations. Considerations of non-trivial spatial topology go back to as early as 1900 by Schwarzschild (Schwarzschild 1900) (English translation (Stewart et al. 1998)). In 1917 de Sitter noted that Einstein's equations of general relativity did not constrain the global structure of the spacetime (de Sitter 1917), while in 1924, Friedmann realized that non-positive curvature spaces could also have compact topology (Friedmann 1924). A number of other papers were published in the following years (for reviews on cosmic topology see, e.g. (Lachieze-Rey & Luminet 1995; Luminet 2008; Starkman 1998; Reboucas & Gomero 2004; Roukema 2000; Blanloeil & Roukema 2000; Levin 2002; Barrow & Kodama 2001), and references therein) but the subject remained purely speculative until very recent accurate measurements of the CMB (cosmic microwave background) anisotropies by the COBE (Bennett et al. 1996) and WMAP (Jarosik et al. 2011; Larson et al. 2011; Komatsu et al. 2011) satellites, and other observational advances in astrophysics and cosmology.

Various models for the topology of the universe (for the classification of different possible topologies see, e.g. (Barrow & Kodama 2001)) have been extensively studied recently and compared to the experimental data. The two most important ones are the Poincaré dodecahedral space and the 3-torus \mathbb{T}^3 ; these models are in best agreement with the experimental data. The Poincaré dodecahedral space arises by slicing the 3-sphere S^3 and thus has positive curvature, while the 3-torus is obtained by slicing infinite Euclidean space \mathbb{R}^3 and therefore is flat. Theoretical arguments about quantum creation of the universe favor the flat case. Based on the Wheeler-DeWitt equation, Linde has argued (Linde 2004) (see also (Zeldovich & Starobinsky 1984)) that compact flat universes are much easier to create than other models, and can naturally provide initial conditions for the onset of inflation. Furthermore, Roukema constructed a measure on the set of compact manifolds and showed that non-flat models almost never occur while flat models occur almost certainly (Roukema & Blanloeil

2010) (see also (Roukema 2010) for a discussion of the Poincaré dodecahedral space versus the 3-torus). Following these arguments, we will focus our attention entirely on the flat case in this work. Details on the Poincaré dodecahedral space and experimental data analysis are given in (Luminet et al. 2003; Roukema 2009; Roukema et al. 2004, 2008; Caillerie et al. 2007; Lew & Roukema 2008; Aurich et al. 2005b), and other topologies in (Aurich & Lustig 2010; Niarchou & Jaffe 2007; Aurich et al. 2006, 2005a; Cresswell et al. 2006; Aurich et al. 2005c; Roukema 2005; Aurich et al. 2004; Riazuelo et al. 2004; Gomero et al. 2002a; Bond et al. 2000; Mota et al. 2005; Gundermann 2005).

We analyze three different flat topologies in this work, $\mathcal{M}_0 = \mathbb{T}^3$, $\mathcal{M}_1 = \mathbb{T}^2 \times \mathbb{R}^1$, and $\mathcal{M}_2 = S^1 \times \mathbb{R}^2$, where the subscript denotes the number of non-compact directions. We will generically refer to all three cases as a torus. Usual flat space is $\mathcal{M}_\infty = \mathbb{R}^3$. The topology of the 3-torus \mathbb{T}^3 can be obtained by identifying the opposite edges of a parallelepiped. We only consider the simplest case of a rectangular parallelepiped with equal side lengths L . This has the highest number of symmetries which helps reduce the computational time. Moreover, it has been argued in (Weeks et al. 2004) that only in well-proportioned spaces is the quadrupole of the CMB temperature-temperature correlation function suppressed compared to the infinite universe. The surprisingly low observed quadrupole is one of the motivations to invoke a compact topology. For our case of the 3-torus, well-proportioned means that all three sides should be approximately equal. The topologies of the spaces $\mathbb{T}^2 \times \mathbb{R}^1$ and $S^1 \times \mathbb{R}^2$ are obtained by compactifying only 2 or 1 dimension respectively. Again, following the argument of (Weeks et al. 2004) and for the sake of simplicity, we consider only the case where the compactified dimensions of $\mathbb{T}^2 \times \mathbb{R}^1$ have the same size. The size of the compact directions will be denoted by L . As $L \rightarrow \infty$ all three manifolds reduce to infinite flat space \mathbb{R}^3 .

Different approaches have been proposed for extracting information about the topology of the universe from the experimental data, the two most important ones being the circles-in-the-sky test and the analysis of the CMB power spectrum. The basic idea of the circles-in-the-sky test is that if the global structure of the space is smaller than the distance to the LSS (last scattering

surface), then the LSS will self-intersect in circles, producing correlations between circles with different centers. The detection of such circles can reveal the global properties of space (for detailed description of the method see, e.g. (Cornish et al. 1998; Mota et al. 2010, 2008; Levin 2004a,b)). The main disadvantage of the method is that it cannot be used if the size of the universe is bigger than the observable part of it (the distance to LSS). The one-year WMAP data has been analyzed with this method for signatures of non-trivial spatial topology (Cornish et al. 2004), ruling out the possibility of compact spaces with a length-scale smaller than 24 Gpc. This limit has been extended by about 10% by the authors of (Shapiro Key et al. 2007) who have also ruled out the possibility of Poincaré dodecahedral space. The authors of (Bielewicz & Banday 2011) have analyzed the most recent seven-year WMAP data with this method, putting a lower bound of about 27.9 Gpc on the size of the fundamental domain for a flat universe.

The low- l (i.e. large scale) portion of CMB correlations is sensitive to the topology of space, which gives rise to another method for detecting the topology. The torus preserves the homogeneity of infinite space but breaks rotational invariance. This implies that the power spectrum of CMB temperature-temperature correlations does not contain all the possible information since the off-diagonal elements of the covariance matrix in the spherical harmonics expansion are non-zero in general, while the diagonal elements with equal l and different m values are not all equal to each other (see section 3 for more details). Moreover, in (Phillips & Kogut 2006) it has been argued that the off-diagonal elements contain more information than the diagonal ones if the side length of the torus is less than twice the distance to the last scattering surface. Therefore, to gain all the possible information from the correlations of CMB anisotropies, one has to consider the full covariance matrix rather than just the power spectrum.

The CMB correlation functions have been previously used to analyze COBE (de Oliveira Costa & Smoot 1995; de Oliveira-Costa et al. 1996), one-year WMAP (Phillips & Kogut 2006; Kunz et al. 2006) and three-year WMAP (Aurich et al. 2008) data. The lower bound on the side length L of \mathbb{T}^3 obtained from COBE data (de Oliveira Costa & Smoot 1995) is $L > 4.32h^{-1}$ Gpc at 95% confidence, and $L > 5.88h^{-1}$ Gpc at 68% confidence. For $\mathbb{T}^2 \times \mathbb{R}^1$ and $S^1 \times \mathbb{R}^2$ the lower bound obtained from COBE (de Oliveira-Costa et al. 1996) is $L > 3.0h^{-1}$ Gpc at 95% confidence. The authors of (Phillips & Kogut 2006) have obtained higher bounds for \mathbb{T}^3 ; $L > 1.2L_0$ at 95% confidence and $L > 2.1L_0$ at 68% confidence.¹ They have also found that the maximum likelihood occurs for $L = 2.1L_0$ (29 Gpc). Several models of tori with different side lengths have been considered in (Kunz et al. 2006) with the conclusions $L > 19.3$ Gpc for \mathbb{T}^3 and $L > 14.4$ Gpc for $S^1 \times \mathbb{R}^2$. The main result of (Aurich et al. 2008) is that the 3-torus with volume $\approx 5 \times 10^3$ Gpc³ (which corresponds to side length of 17 Gpc) is well-compatible with the WMAP three-year

data. The WMAP seven-year data has been analyzed for detecting signatures of the so-called half-turn space (Aurich & Lustig 2010) (the only difference of the half-turn space from the 3-torus is that one of the edges is turned by 180° before identifying with the opposite edge) where the case of the 3-torus is also considered. Out of these works, only in (Phillips & Kogut 2006) and (Kunz et al. 2006) has the full covariance matrix been analyzed. For some earlier results on these topologies see also (Starobinsky 1993; Sokolov 1993; Stevens et al. 1993) and references therein.

Other methods for experimental detection of non-trivial topologies have been proposed and used to analyze the experimental data. The so-called spatial cross-correlation function method has been used in (Aurich 2008) to analyze the five-year WMAP data for signatures of a 3-torus topology with a result $L = 3.85H_0^{-1}$. They have also specified the orientation of the torus. In (Bielewicz & Riazuelo 2008) multipole vectors have been used to analyze the five-year WMAP data with the conclusion that a torus topology is slightly preferred. The authors of (Menzies & Mathews 2005) have looked for evidence for a 3-torus topology by the alignment of distant objects. They have put a lower bound on the side length $L > 0.9L_0$. For some other approaches see also (Hipolito-Ricaldi & Gomero 2005; Marecki et al. 2005; Gomero 2003; Hajian & Souradeep 2003; Opher 2004; Dineen et al. 2005; Gomero et al. 2000; Reboucas 2000; Gomero et al. 2001; Gomero 2002; Gomero et al. 2002b).

In this work we analyze the most recent seven-year WMAP data for signatures of the three flat topologies of space mentioned above using the full covariance matrix of temperature-temperature fluctuations. By using the symmetry groups of the spaces we construct efficient algorithms for the theoretical computation of the covariance matrix and the likelihood function using that matrix. These algorithms can be used again as soon as the high precision data from the Planck satellite (Planck Collaboration 2006) are released. The computation of the covariance matrix is done using a modified version of the CAMB program (Lewis et al. 2000), as discussed in Sec. 3, and that of χ^2 and the likelihood using the available WMAP code (Jarosik et al. 2011; Larson et al. 2011; Komatsu et al. 2011). We have used only the TT correlations in our analysis. Including TE , EE , and BB correlations is straightforward, but would quadruple the computer time needed, without much improvement in the results since these other correlations have much larger errors.

There have been speculations in the literature about the detection of a special direction in the CMB map in which the first few multipoles of temperature-temperature correlations seem to be aligned (Land & Magueijo 2005, 2007; Rakic & Schwarz 2007). This is referred to as the “axis of evil” and is given by $b = 60^\circ$, $l = -100^\circ$ in galactic coordinates. The topologies that we consider are not rotationally invariant, in particular $\mathbb{T}^2 \times \mathbb{R}^1$, and $S^1 \times \mathbb{R}^2$ have one special direction (the infinite one in $\mathbb{T}^2 \times \mathbb{R}^1$, and the finite one in $S^1 \times \mathbb{R}^2$), so we analyze the case where this special direction coincides with the axis of evil, to see if the axis of evil can be explained by one of these topologies. The authors of (Cresswell et al. 2006) have

¹ We will give lengths in terms of $L_0 = 14.4$ Gpc, the distance to the last scattering surface. The Hubble length is $H_0^{-1} = 2.998/h_0 = 4.266(0.703/h_0)$ Gpc.

analyzed the topology $S^1 \times \mathbb{R}^2$ with the conclusion that it is not the explanation for the multipole alignment.

The work is organized as follows. In section 2 we present a slight generalization of Linde’s argument for the quantum creation of compact universes. We describe the calculation of the covariance matrix and the likelihood in sections 3 and 4 respectively. We present our numerical results in section 5, and discuss the goodness of fit, and maximum likelihood confidence intervals. We have done several checks of our analysis, which are given in Sec. 6. The possibility that our results are generated by a random fluctuation are analyzed in section 7, where we discuss Monte-Carlo skies. The possibility of spurious effects due to a small residual CMB dipole in the data is investigated in Sec. 8. We summarize in section 9. Unless otherwise stated, everywhere in this work the side length of the torus is given in units of the distance to the last scattering surface L_0 .

2. QUANTUM CREATION OF COMPACT UNIVERSES

Consider the standard Einstein-Hilbert action of gravity minimally coupled to matter. Here we will be only interested in “quantizing” gravity, so for the matter portion we will just consider energy density V without worrying about where it comes from. Then the action takes the form ($\hbar = c = 1$, $M_{pl} \equiv (8\pi G)^{-1/2} = 1$)

$$S = \frac{1}{2} \int d^4x \sqrt{-g} (R - 2V). \quad (1)$$

Following the standard procedure to derive the Wheeler-DeWitt equation we use the ADM form of the spacetime metric (Arnowitt et al. 2008)

$$ds^2 = -N^2 dt^2 + h_{ij} (dx^i + N^i dt) (dx^j + N^j dt). \quad (2)$$

The action can be rewritten in the form

$$S = \int d^4x \mathcal{L}, \quad (3)$$

with

$$\mathcal{L} = \frac{\sqrt{\hbar} N}{2} \left({}^3R + \frac{1}{N^2} (E_{ij} E^{ij} - E^2) - 2NV \right) \quad (4)$$

where 3R is the 3-curvature of spatial slices,

$$\begin{aligned} E_{ij} &= \frac{1}{2} (\dot{h}_{ij} - \nabla_i N_j - \nabla_j N_i), \\ E &= E^i_i. \end{aligned} \quad (5)$$

There are numerous possibilities for the spacetime manifold and it may be described by infinitely many parameters, so to be able to proceed we consider manifolds with finite homogeneous spatial slices which can be characterized by one length scale $a(t)$. In other words, we assume that locally the manifold is characterized by a Friedmann-Robertson-Walker metric while globally it can have any finite topology that is compatible with the metric. So by a suitable choice of coordinates we get in this case

$$N = 1, \quad N_i = 0, \quad (6)$$

$$h_{ij} = a^2(t) k_{ij}, \quad (7)$$

where the tensor k_{ij} is constant (it only depends on the choice of the manifold but does not depend on any of the

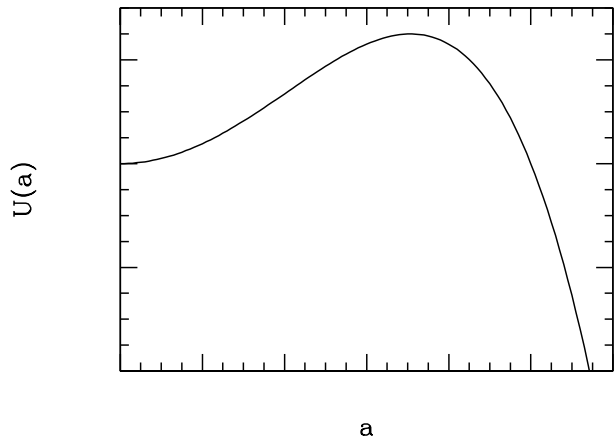


FIG. 1.— Plot of the potential $U(a)$ for a positively curved space ($\beta > 0$). The axes are in arbitrary units.

coordinates). Then

$$E_{ij} E^{ij} - E^2 = -6 \left(\frac{\dot{a}}{a} \right)^2. \quad (8)$$

Since we assumed a homogeneous spatial submanifold characterized by single length scale a , by dimensional analysis the volume must be proportional to a^3 and the curvature to a^{-2} . Namely,

$$\int d^3x \sqrt{h} = \alpha a^3, \quad (9)$$

$${}^3R = \frac{\beta}{a^2}, \quad (10)$$

where α and β are dimensionless constants that depend only on the choice of the manifold. The Lagrangian then takes the form

$$L = \frac{\alpha}{2} (a\beta - 6a\dot{a}^2 - 2a^3V). \quad (11)$$

Now we treat a as the dynamical variable describing the geometry. The canonical momentum is then

$$p_a = \frac{\partial L}{\partial \dot{a}} = -6\alpha a \dot{a}, \quad (12)$$

and the Hamiltonian becomes

$$H = p_a \dot{a} - L = \frac{1}{12\alpha a} (-p_a^2 - 6\alpha^2 \beta a^2 + 12\alpha^2 a^4 V). \quad (13)$$

Finally, we canonically quantize, replacing p_a by the operator $-i(d/da)$ to get for the Hamiltonian

$$H = \frac{1}{12\alpha a} \left(\frac{d^2}{da^2} - 6\alpha^2 \beta a^2 + 12\alpha^2 a^4 V \right). \quad (14)$$

Consider now the quantum creation of the universe with zero energy. Then the wavefunction of the universe $\Psi(a)$ satisfies the analog of the Schrödinger equation with Hamiltonian Eq. (14), which is called the Wheeler-DeWitt equation. In this case it takes the form

$$\left(\frac{d^2}{da^2} - 6\alpha^2 \beta a^2 + 12\alpha^2 a^4 V \right) \Psi(a) = 0. \quad (15)$$

The effective potential energy is

$$U(a) = 6\alpha^2 \beta a^2 - 12\alpha^2 a^4 V, \quad (16)$$

and is shown in Fig. 1 which decreases to $-\infty$ for large

a since the second term dominates. However, for small a the first term dominates, so for $\beta > 0$ there is a potential barrier from $a = 0$ to $\sqrt{\beta/2V}$, i.e. the universe has to first undergo tunneling before the expansion can start. This is the reason why the probability of quantum creation of positively curved spaces, which have $\beta > 0$, is thought to be highly suppressed compared to flat and negatively curved spaces. The action for tunneling through the barrier is $S = a_0^3 \sqrt{V}/3$, where $a_0 = \sqrt{\beta/(2V)}$ is the size of the created universe. The tunneling probability is $\propto \exp(-S)$, and is greater for smaller universes; $S \rightarrow 0$, $a_0 \rightarrow 0$ as $V \rightarrow \infty$. For a flat universe, $\beta = 0$, and the barrier vanishes.

3. COVARIANCE MATRIX CALCULATION

Now we turn to the calculation of correlations between CMB temperature anisotropies in the flat topologies \mathbb{T}^3 , $\mathbb{T}^2 \times \mathbb{R}^1$, and $S^1 \times \mathbb{R}^2$. Locally they all look exactly like the infinite flat \mathbb{R}^3 so Einstein's equations and therefore the Friedmann equations are unchanged from the infinite case. The calculation for the infinite case is described in standard textbooks (for a detailed derivation see (Dodelson 2003)), so let us briefly summarize that calculation and then focus on the differences between the infinite and finite universes. Essentially, one has to take the Einstein's equations that describe the interactions between gravity and all of matter and Boltzmann's equations for interactions between various types of matter (most importantly, electrons and photons) and solve for the distribution of photons today given initial conditions set by inflation. Since the temperature anisotropies in the CMB are about five orders of magnitude smaller than the background, the calculation is done using perturbation theory around the homogeneous background and keeping only first order terms. Then all of the differential equations become linear and can be treated easily in Fourier space. This is where there is a key difference: in an infinite universe the spectrum of the Fourier modes \mathbf{k} is continuous, while for compactified dimensions the spectrum becomes discrete. For a torus with side lengths L_1 , L_2 , and L_3 we have $\mathbf{k} = (k_1, k_2, k_3)$,

$$k_1 = \frac{2\pi}{L_1} n_1, \quad k_2 = \frac{2\pi}{L_2} n_2, \quad k_3 = \frac{2\pi}{L_3} n_3, \quad (17)$$

where n_1, n_2, n_3 are integers (the torus is essentially a box with periodic boundary conditions). So all of the equations in Fourier space remain unchanged, all we have to worry about is integrations over \mathbf{k} which have to be replaced by sums

$$\int \frac{d^3k}{(2\pi)^3} \rightarrow \frac{1}{L_1 L_2 L_3} \sum_{\mathbf{k}}, \quad (18)$$

over the discrete \mathbf{k} values in Eq. (17). The set of points Eq. (17) will be referred to as the \mathbf{k} grid.

The three cases studied here can be characterized by different values for L_i . The three-torus \mathbb{T}^3 has $L_1 = L_2 = L_3 = L$, $\mathbb{T}^2 \times \mathbb{R}^1$ has $L_1 = L_2 = L$, $L_3 = \infty$, and finally $S^1 \times \mathbb{R}^2$ has $L_1 = L_2 = \infty$, $L_3 = L$. All three cases can be treated in a unified manner by using the integral

notation, with the understanding that the integral is to be replaced by a summation if the corresponding L_i is finite.

The first set of summations over \mathbf{k} arises when constructing collision terms in Boltzmann's equations. However, we will not worry about these integrals for the following reason. The Boltzmann's equations are important only before the decoupling epoch, which corresponds to a redshift of about $z \sim 1100$. The comoving horizon at that time was about 50 times bigger than currently, and the current bounds on the size of the torus are of the order of the size of horizon, so at the epoch of decoupling, the size of the torus was at least about 50 times bigger than the causally connected part. As we will see later in section 5, the sums rapidly converge to the corresponding integrals when the topology scale is around 3 times the radius of horizon, which implies that the effects of finiteness can be safely ignored for the epoch of decoupling (and before), and \mathbf{k} can be treated as a continuous variable. All the equations are solved in Fourier space, exactly as for the infinite case.

There is a summation over \mathbf{k} when the final answer for the temperature fluctuations has to be converted from Fourier space back to real space. So let us pick up from that point in the calculation. The temperature anisotropies $\Theta(\hat{\mathbf{n}}, \mathbf{x})$ in direction $\hat{\mathbf{n}}$ at a given point \mathbf{x} (chosen to be our location \mathbf{x}_0) are decomposed into spherical harmonics

$$\Theta(\hat{\mathbf{n}}, \mathbf{x}) = \sum_{l=1}^{\infty} \sum_{m=-l}^l a_{lm}(\mathbf{x}) Y_{lm}(\hat{\mathbf{n}}), \quad (19)$$

where the position space a_{lm} coefficients are given in terms of the Fourier space temperature fluctuations $\Theta(\hat{\mathbf{n}}, \mathbf{k})$ by

$$a_{lm}(\mathbf{x}) = \int \frac{d^3k}{(2\pi)^3} e^{i\mathbf{k}\cdot\mathbf{x}} \int d\Omega Y_{lm}^*(\hat{\mathbf{n}}) \Theta(\hat{\mathbf{n}}, \mathbf{k}). \quad (20)$$

The observed CMB fluctuations are given by the correlations between the different a_{lm} 's,

$$M_{lm'l'm'} \equiv \langle a_{lm}(\mathbf{x}_0) a_{l'm'}^*(\mathbf{x}_0) \rangle. \quad (21)$$

The correlations between temperature anisotropies in k -space are related to the initial matter power spectrum

$$\begin{aligned} & \langle \Theta(\mathbf{k}, \hat{\mathbf{n}}) \Theta^*(\mathbf{k}', \hat{\mathbf{n}}') \rangle \\ &= (2\pi)^3 \delta^3(\mathbf{k} - \mathbf{k}') P(k) \frac{\Theta(k, \mathbf{k} \cdot \hat{\mathbf{n}})}{\delta(k)} \frac{\Theta^*(k, \mathbf{k} \cdot \hat{\mathbf{n}}')}{\delta^*(k)}, \end{aligned} \quad (22)$$

where the matter power spectrum is defined by (Dodelson 2003)

$$\langle \delta(\mathbf{k}) \delta^*(\mathbf{k}') \rangle \equiv (2\pi)^3 \delta^3(\mathbf{k} - \mathbf{k}') P(k). \quad (23)$$

The ratios Θ/δ on the right hand side of Eq. (22) do not depend on the initial conditions since the equations are linear. All of the information about initial conditions is now absorbed into $P(k)$. From Eq. (20), (21), and (22) we get

$$M_{lm'l'm'} = \int \frac{d^3k}{(2\pi)^3} P(k) \int d\Omega Y_{lm}^*(\hat{\mathbf{n}}) \frac{\Theta(k, \mathbf{k} \cdot \hat{\mathbf{n}})}{\delta(k)} \int d\Omega' Y_{l'm'}(\hat{\mathbf{n}}') \frac{\Theta^*(k, \mathbf{k} \cdot \hat{\mathbf{n}}')}{\delta^*(k)}. \quad (24)$$

Expanding $\Theta(k, \mathbf{k} \cdot \hat{\mathbf{n}})$ into Legendre polynomials

$$\Theta(k, \mathbf{k} \cdot \hat{\mathbf{n}}) = \sum_l (-i)^l (2l+1) P_l(\hat{\mathbf{k}} \cdot \hat{\mathbf{n}}) \Theta_l(k), \quad (25)$$

and using the identity

$$\int d\Omega P_{l'}(\hat{\mathbf{k}} \cdot \hat{\mathbf{n}}) Y_{lm}(\hat{\mathbf{n}}) = \frac{4\pi}{2l+1} \delta_{ll'} Y_{lm}(\hat{\mathbf{k}}), \quad (26)$$

we finally get

$$M_{lm'l'm'} = (4\pi)^2 (-i)^l i^{l'} \times \int \frac{d^3k}{(2\pi)^3} P(k) \frac{\Theta_l(k)}{\delta(k)} \frac{\Theta_{l'}^*(k)}{\delta^*(k)} Y_{lm}^*(\hat{\mathbf{k}}) Y_{l'm'}(\hat{\mathbf{k}}). \quad (27)$$

We first review the standard result for an infinite universe. In this case, the angular part of the integral over \mathbf{k} in Eq. (27) can be done analytically giving

$$M_{lm'l'm'} = \delta_{ll'} \delta_{mm'} C_l, \quad (28)$$

with

$$C_l = \frac{2}{\pi} \int dk k^2 P(k) \left| \frac{\Theta_l(k)}{\delta(k)} \right|^2. \quad (29)$$

The derivation remains the same in the finite case except that the \mathbf{k} integral must be replaced by the sum Eq. (18), so instead of Eq. (27) we get

$$M_{lm'l'm'} = (4\pi)^2 (-i)^l i^{l'} \times \frac{1}{L_1 L_2 L_3} \sum_{\mathbf{k}} P(k) \frac{\Theta_l(k)}{\delta(k)} \frac{\Theta_{l'}^*(k)}{\delta^*(k)} Y_{lm}^*(\hat{\mathbf{k}}) Y_{l'm'}(\hat{\mathbf{k}}). \quad (30)$$

Now we have to compute a three-dimensional sum Eq. (30) instead of a one-dimensional integral Eq. (29) which requires much more computational time. Also, we have to calculate all matrix elements with different l, m, l', m' whereas in the infinite case all $l \neq l'$ or $m \neq m'$ (non-diagonal) elements vanish, while the diagonal ones do not depend on m . The reason for this is clear. In the infinite case, the problem has full rotational invariance, so that angular momentum is conserved. In the cases we consider, rotational invariance is broken. Even though rotational invariance is broken, there is still a large residual discrete symmetry group which can be used to simplify the problem, and reduce the computational time. We will refer to this residual symmetry group as G . For the $\mathbb{T}^2 \times \mathbb{R}^1$ and $S^1 \times \mathbb{R}^2$ cases, G is the symmetry group of a rectangular parallelepiped with two sides equal, the tetragonal group D_{4h} with 16 elements, whereas for \mathbb{T}^3 , G is the symmetry group of the cube, the octahedral group O_h with 24 elements.

The angular part in the sum in Eq. (30) can be separated (this has been suggested earlier in (Phillips & Kogut 2006))

$$M_{lm'l'm'} = \frac{(4\pi)^2 (-i)^l i^{l'}}{L_1 L_2 L_3} \sum_{\mathbf{k}} P(k) \frac{\Theta_l(k)}{\delta(k)} \frac{\Theta_{l'}^*(k)}{\delta^*(k)} \times \sum_{|\mathbf{k}|=k} Y_{lm}^*(\hat{\mathbf{k}}) Y_{l'm'}(\hat{\mathbf{k}}), \quad (31)$$

where the first sum is over all the allowed spheres in the \mathbf{k} grid while the angular sum is over a fixed sphere and depends only on the choice of that sphere.

We can simplify the computation using the discrete symmetry group G of the manifolds $\mathcal{M}_{0,1,2}$. Consider a

fixed sphere of radius k . If the point (θ, ϕ) of the sphere is on the grid, then so are $(\theta, \phi + \pi/2)$, $(\theta, \phi + \pi)$, and $(\theta, \phi + 3\pi/2)$. The angular sum over these four points is proportional to

$$e^{i(m'-m)\phi} \left(1 + e^{i(m'-m)\frac{\pi}{2}} + e^{i(m'-m)\pi} + e^{i(m'-m)\frac{3\pi}{2}} \right),$$

which is 0 unless $m' - m$ is divisible by 4, in which case it becomes $4e^{i(m'-m)\phi}$. Consider the points (θ, ϕ) and $(-\theta, \phi)$, which both lie on the sphere. Since

$$Y_{lm}(-\theta, \phi) = (-1)^{l-m} Y_{lm}(\theta, \phi),$$

the sum over those two points is 0 unless $l + l' - m - m'$ is even, but $m + m'$ is even if $m' - m$ is divisible by 4, so the extra condition we get is that $l' - l$ has to be even (this also follows from parity). The eight points $(\pm\theta, \phi + n\pi/2)$, $n = 0, 1, 2, 3$ lie in the eight different octants, so the point (θ, ϕ) can be chosen to lie in the first octant. To summarize, the angular sum is nonzero only if $l' - l$ is even and $m' - m$ is divisible by 4, in which case it is equal to 8 times the sum over one octant. Extra care is needed for points on the boundary of the octant to avoid double counting.

Consider the points (θ, ϕ) and $(\theta, \pi/2 - \phi)$ corresponding to swapping n_1 with n_2 . Taking into account that $m' - m$ is divisible by 4, we get

$$e^{i(m'-m)\phi} + e^{i(m'-m)(\frac{\pi}{2}-\phi)} = 2 \cos((m' - m)\phi),$$

which implies that the angular sums are real. Furthermore, $(-i)^l i^{l'}$ is also real for even $l' - l$ and $P(k)$ and $\Theta_l(k)/\delta(k)$ are real, so the covariance matrix elements $M_{lm'l'm'}$ are all real implying $M_{lm'l'm'} = M_{l'm'l'm}$. Also, since $Y_{l,-m}(\theta, \phi) = (-1)^m Y_{lm}^*(\theta, \phi)$ and $m' - m$ is divisible by 4, we get $M_{lm'l'm'} = M_{l,-m,l',-m'}$.

\mathbb{T}^3 has more symmetries which can be used to further speed up the calculation for this case. For example, the sums in Eq. (31) over the spherical harmonics are the same for all L . Changing L is a rescaling of the allowed momenta by $1/L$. Thus the angular sum for $|\mathbf{k}| = k$ for a \mathbb{T}^3 of size L is the same as the angular sum for $|\mathbf{k}| = \lambda k$ for \mathbb{T}^3 of size L/λ . Thus the angular sums can be computed once, and then used for all values of L .

Since the calculation of $\Theta_l(k)/\delta(k)$ is identical to the case of infinite flat universe, we use the well-known CAMB software (Lewis et al. 2000) (based on CMBFAST (Seljak & Zaldarriaga 1996)) for that part of the calculation. Our code is essentially a modification of CAMB. It takes the sides of the torus as extra input parameters and outputs not only C_l but also the complete matrix $M_{lm'l'm'}$. For large values of l , the discrete sums over \mathbf{k} approach the continuum result, so we only use Eq. (31) for $l \leq 30$, and use the continuum result for $l > 30$. The difference between the discrete and continuum values for $M_{lm'l'm'}$ is less than 0.5% for $l = 30$. As an example, in Fig. 2, we have plotted the ratio of the power spectrum C_l for $\mathcal{M}_1 = \mathbb{T}^2 \times \mathbb{R}^1$ with $L/L_0 = 1.9$ to that for infinite space \mathbb{R}^3 , where C_l has been defined as

$$C_l = \frac{1}{2l+1} \sum_{m=-l}^l M_{lmlm} \quad (32)$$

for $\mathcal{M}_1 = \mathbb{T}^2 \times \mathbb{R}^1$. The $l = 2$ power is reduced by 7%, and the ratio of power spectra oscillates and rapidly approaches unity. The two differ by 0.1% at $l = 30$.

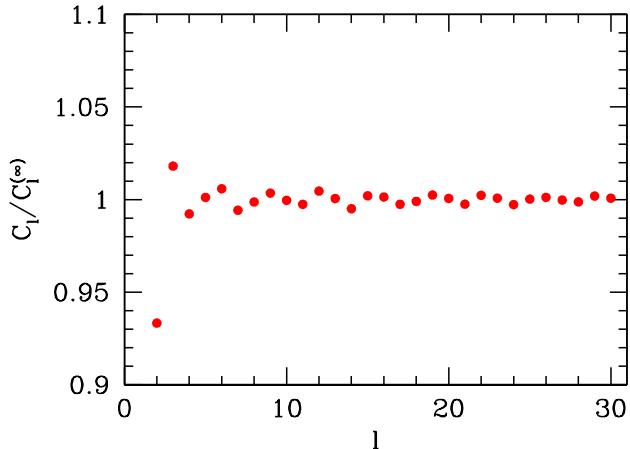


FIG. 2.— Plot of the ratio of C_l for $\mathcal{M}_1 = \mathbb{T}^2 \times \mathbb{R}^1$ with $L/L_0 = 1.9$, to that for infinite space \mathbb{R}^3 .

4. LIKELIHOOD CALCULATION

The matrix $M_{lm'l'm'}$ computed as discussed above is compared to the experimental data from the 7-year WMAP survey. Since rotational invariance is broken, we need to vary the orientation of the torus relative to axes fixed in space, to find the best fit. We do this by rotating the data relative to the torus in computing the likelihood function. We specify the orientation by three Euler angles (ϕ, θ, ψ) in the following way. The axes x, y, z are fixed in the coordinate frame of the CMB data, i.e. the observed universe, and the x', y', z' axes are fixed in the torus. Start with the CMB-fixed and torus-fixed axes aligned. Rotate the torus counterclockwise around the z -axis by angle ϕ , then around the *new* x -axis by angle θ , then around the *new* z -axis by angle ψ to get the final torus orientation. The angles ϕ and θ give the orientation of the z -axis of the torus while the angle ψ gives the orientation of the torus around its z -axis. We can make use of the symmetries of our topologies to speed up the calculation since various Euler angles can give equivalent orientations of the torus. Two sets of Euler angles (ϕ, θ, ψ) and (ϕ', θ', ψ') are equivalent if $\exists g \in G$ such that

$$R(\phi, \theta, \psi) = R(g) R(\phi', \theta', \psi') \quad (33)$$

where $R(\phi, \theta, \psi)$ is the coordinate transformation rotation matrix corresponding to (ϕ, θ, ψ) and $R(g)$ is that corresponding to the discrete element g . This defines an equivalence relation on the set of all possible Euler angles. We take a uniform grid on all possible angles, then divide that grid into equivalence classes according to Eq. (33) and take one representative from each class. We have scanned over ~ 4000 inequivalent angles.

Different orientations of the torus were considered in the previous analysis of first-year WMAP data for \mathbb{T}^3 (Phillips & Kogut 2006), but they only considered a uniform grid on the range $0 \leq \phi, \theta, \psi \leq \pi/2$. Note that this does not cover all possible orientations of \mathbb{T}^3 . The first two angles describe the orientation of the z -axis and by their assumption on the range of ϕ, θ, ψ , the z -axis always lies in the first octant. However taking into account all the symmetries of the cube there are 6 equivalent axes that can play the role of the z -axis, the $\pm x$, $\pm y$, and $\pm z$ axes, while there are 8 octants. In other words, there are

possible orientations of the cube for which none of the 6 axes lies in the first octant.

After choosing a torus orientation, we calculate the likelihood in the real space of orientations on the last scattering surface. For N_p pixels the likelihood function is given by² (Dodelson 2003)

$$\mathcal{L} = \frac{1}{(2\pi)^{N_p/2} (\det C)^{1/2}} \exp\left(-\frac{1}{2} \Delta^T C^{-1} \Delta\right), \quad (34)$$

and the χ^2 function by

$$\chi^2 = \Delta^T C^{-1} \Delta, \quad (35)$$

where Δ_i is the vector of pixels and C_{ij} is the covariance matrix that also includes the noise. The indices i, j label the different pixels, which are in directions $\hat{\mathbf{n}}_{i,j}$ on the sky.

We now describe how to convert the matrix $M_{lm'l'm'}$ to the covariance matrix C_{ij} . The temperature fluctuation measured in a pixel i is given by (Dodelson 2003)

$$\Theta_i = \int d\hat{\mathbf{n}} \Theta(\hat{\mathbf{n}}) B_i(\hat{\mathbf{n}}), \quad (36)$$

where B_i is the beam pattern at the pixel i and is specific to the experiment. Usually the beam patterns have the same shape for every pixel and are axially symmetric around the center of the pixel, as is the case for WMAP, so if we denote the direction to the center of the pixel by $\hat{\mathbf{n}}_i$ then the beam pattern can be decomposed into spherical harmonics

$$B_i(\hat{\mathbf{n}}) = \sum_{lm} B_l Y_{lm}(\hat{\mathbf{n}}_i) Y_{lm}^*(\hat{\mathbf{n}}). \quad (37)$$

Using Eq. (19) to decompose $\Theta(\hat{\mathbf{n}})$ into spherical harmonics, we get for the theoretical covariance matrix

$$C_{ij} \equiv \langle \Theta_i \Theta_j \rangle = \sum_{lm'l'm'} M_{lm'l'm'} B_l B_{l'} Y_{lm}(\hat{\mathbf{n}}_i) Y_{l'm'}^*(\hat{\mathbf{n}}_j). \quad (38)$$

In computing C_{ij} , we have to vary the orientation of the torus relative to the sky. In implementing the Euler angle rotation, one can compute the $M_{lm'l'm'}$ matrix in the torus-fixed coordinate system, so that it remains unchanged as the Euler angles are varied. The pixel directions \mathbf{n}_i are changed to $\mathbf{n}_i \rightarrow R(\phi, \theta, \psi) \mathbf{n}_i$. Equivalently, one can work in the CMB-fixed coordinate system, and rotate the torus, which gives $M_{lm'l'm'}$ transformed by the angular momentum rotation matrices,

$$M_{lm'l'm'} \rightarrow \sum_{n,n'} M_{lnl'n'} D_{nm}^{(l)*}(R) D_{n'm'}^{(l)}(R). \quad (39)$$

Note that in the infinite universe case, Eq. (28) holds, and the result Eq. (38) simplifies to

$$C_{ij} = \sum_l \frac{4\pi}{2l+1} B_l^2 C_l P_l(\hat{\mathbf{n}}_i \cdot \hat{\mathbf{n}}_j), \quad (40)$$

independent of the rotation $R(\phi, \theta, \psi)$.

The computation of the covariance matrix using Eq. (38) is more involved than the infinite case, Eq. (40), so the likelihood calculations require far more computer

² To distinguish from length scale L , the likelihood is denoted by \mathcal{L} everywhere in this work.

time than the conventional case. C_{ij} must be recalculated for each set of Euler angles. There are 458403 independent elements in $M_{lm'l'm'}$ for $2 \leq l \leq 30$ of which 57840 satisfy the $l \equiv l' \pmod{2}, m \equiv m' \pmod{4}$ condition, and 2482 values for each of the indices i and j . The slowest step in the computation is evaluating the sums on l, m, l', m' in Eq. (38) for all values of $\{i, j\}$.

An Euler angle rotation of the sky maps points on the sphere to rotated points on the sphere. For infinitesimal pixels, this corresponds to a reshuffling of the pixels, i.e. if pixel i at \mathbf{n}_i is mapped by the rotation to \mathbf{n}_j , then pixel $i \rightarrow$ pixel j . An exact reshuffling of pixels would greatly simplify the computation — instead of recomputing C_{ij} , one could simply permute the indices on C_{ij} to get the transformed matrix. In particular, $\det C$ would remain invariant under this transformation.

The WMAP pixels have been chosen using the HEALPix grid (Gorski et al. 2005). The pixels are chosen to lie along lines of constant latitude, and they have equal solid angles. This implies that the spacing of the pixels varies as a function of latitude. As a result one cannot treat rotations of the sky as a pixel reshuffling transformation. One can approximate the rotations by a pixel transformation by mapping the rotated pixel to the one closest to it in the HEALPix grid. The likelihood computed using this method differs from the exact result using Eq. (38), and is not accurate enough for our purposes. The above approximate relation between rotations and pixel permutations does, however, explain why $\det C$ is approximately independent of the Euler angles.

For a finite universe, one has to use Eq. (38) with the value for $M_{lm'l'm'}$ computed as described in Sec. 3. The finiteness of the universe only affects the large-scale anisotropies, so the difference between the infinite and finite cases goes to zero with increasing l . For that reason we will look only at low- l portion of anisotropies, $l \leq 30$, and use the infinite manifold result Eq. (40) for $l > 30$. We calculate χ^2 and the likelihood \mathcal{L} using a modification of the likelihood code provided by the WMAP team (Jarosik et al. 2011; Larson et al. 2011; Komatsu et al. 2011) as a function of the new parameters (L, ϕ, θ, ψ) . Since we are interested only in low- l effects we use the low-resolution portion of the likelihood code. We use the experimental data in the exact same form as provided by the WMAP team without any further modifications. The temperature map used is the smoothed and degraded ILC map with the Kp2 mask applied to remove the galactic plane and strong point sources. The map originally has 3072 pixels, but only 2482 are left after the mask.

Ideally, one would have to do a fit to the experimental data varying the four new parameters (L, ϕ, θ, ψ) in addition to all the other cosmological parameters. The cosmological parameters affect the whole spectrum of anisotropies while only the low- l part of the spectrum is affected by the new parameters, so we fix the other cosmological parameters at their best-fit values as given by the seven-year WMAP data (Komatsu et al. 2011) and only vary the new parameters. The values of the cosmological parameters that we use are (Komatsu et al. 2011) $100\Omega_b h^2 = 2.227$, $\Omega_c h^2 = 0.1116$, $\Omega_\Lambda = 0.729$, $n_s = 0.966$, $\tau = 0.085$, $\Delta_R^2(0.002 \text{ Mpc}^{-1}) = 2.42 \times 10^{-9}$.

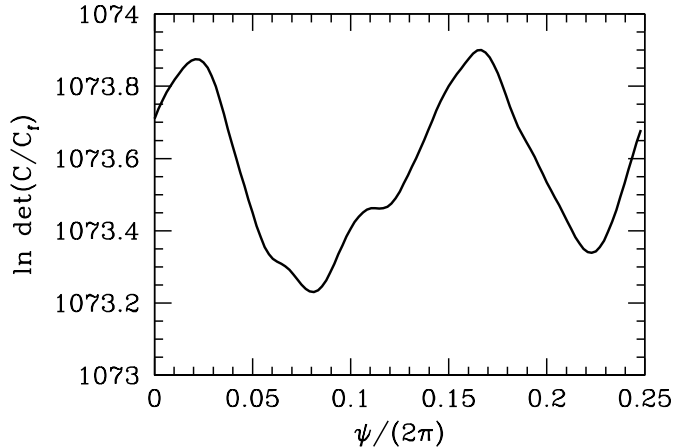


FIG. 3.— Plot of $\ln \det C/C_f$ against the Euler angle ψ for fixed ϕ, θ for the \mathcal{M}_0 topology at $L/L_0 = 1.8$,

5. RESULTS

We have computed the likelihood and χ^2 for the three cases, $\mathcal{M}_0 = \mathbb{T}^3$, $\mathcal{M}_1 = \mathbb{T}^2 \times \mathbb{R}^1$ and $\mathcal{M}_2 = S^1 \times \mathbb{R}^2$, for different values of L/L_0 as a function of the Euler angles. L/L_0 ranges between a minimum value of 0.5 – 1.0 depending on the manifold, and a maximum value of $L/L_0 = 2.6$, in steps of $L/L_0 = 0.1$. By the time $L/L_0 = 2.6$, the results are almost identical to the flat-space case $\mathcal{M}_\infty = \mathbb{R}^3$. For the statistical analysis discussed later in this section, we have used interpolation to construct a smooth function of L .

The relation between likelihood and χ^2 is

$$-2 \ln \mathcal{L} = \chi^2 + \ln \det C/C_f + \ln \det(2\pi C_f) \quad (41)$$

where C_f is a fiducial covariance matrix used by the WMAP collaboration. C_f is independent of L and the Euler angles, and drops out of all likelihood ratios. χ^2 and $-2 \ln \mathcal{L}$ differ by $\ln \det C/C_f$ (up to an irrelevant constant). The likelihood for \mathcal{M}_∞ , three-dimensional flat space, will be denoted by \mathcal{L}_∞ , and is $\mathcal{L}_\infty = 3573.4$

As noted earlier, for fixed L/L_0 , $\ln \det C/C_f$ varies weakly with the Euler angles. In Fig. 3, we have plotted the variation of $\ln \det C/C_f$ as a function of ψ , for fixed values of the ϕ, θ , at $L/L_0 = 1.8$. The overall variation of $\ln \det C/C_f$ against ψ is less than unity.

$-2 \ln \mathcal{L}$ (and hence χ^2) has a strong variation with Euler angles at fixed L/L_0 . In Fig. 4, we have shown plots of the variation of $2 \ln \mathcal{L}_\infty - 2 \ln \mathcal{L}$ with Euler angle ψ for fixed ϕ, θ for the \mathcal{M}_0 topology. \mathcal{L}_∞ is independent of the Euler angles. The solid red curve has been chosen to have $L/L_0 = 1.8$, and ϕ, θ values that maximize the likelihood at this value of L/L_0 . There is a large variation of $-2 \ln \mathcal{L}$ with the remaining Euler angle ψ , and the global minimum of $-2 \ln \mathcal{L}$ is $2 \ln \mathcal{L}_\infty - 2 \ln \mathcal{L} = -17.2$ at $\psi/(2\pi) \approx 0.05$. The strong dependence of $-2 \ln \mathcal{L}$ on orientation makes it difficult to find the true global minimum of the $-2 \ln \mathcal{L}$ and χ^2 functions. We have done a scan over all Euler angles with a spacing of 0.05π , to identify valleys, followed by a finer scan to find the minimum. By comparing our numerical minimum with the next best point, we can estimate the uncertainty in our minimum $-2 \ln \mathcal{L}$ and χ^2 values at less than 0.5. The dashed blue curve in Fig. 4 is also for $L/L_0 = 1.8$, but with ϕ, θ fixed at random values, rather than those for which $-2 \ln \mathcal{L}$

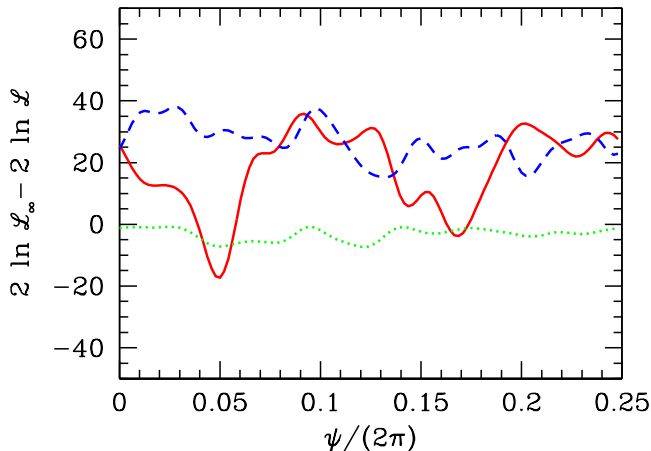


FIG. 4.— Plot of $2 \ln \mathcal{L}_\infty - 2 \ln \mathcal{L}$ against the Euler angle ψ for fixed ϕ, θ for the \mathcal{M}_0 topology. The solid red and dashed blue curves are for two different values of ϕ, θ at $L/L_0 = 1.8$, and the dotted green curve is for $L/L_0 = 2.2$. The solid red curve is for $L/L_0 = 1.8$ with ϕ, θ fixed to be the best fit values, the dashed blue curve is for $L/L_0 = 1.8$ with ϕ, θ fixed in a random direction, and the dotted green curve is for $L/L_0 = 2.2$ with ϕ, θ fixed to be the best fit values.

vs. ψ passes through the global minimum. There is still considerable dependence as one varies the third angle ψ , but the dependence is much weaker than for the solid red curve. The dependence of $-2 \ln \mathcal{L}$ drops rapidly with increasing L/L_0 . For $L/L_0 = 2.2$, the dotted green curve in the figure, the overall variation is about 6.5.

The plot of χ^2 and $-2 \ln \mathcal{L}$ against L/L_0 is given in Figs. 5, 6, 7 for the three cases, $\mathcal{M}_0 = \mathbb{T}^3$, $\mathcal{M}_1 = \mathbb{T}^2 \times \mathbb{R}^1$ and $\mathcal{M}_2 = S^1 \times \mathbb{R}^2$, respectively. We have plotted the maximum and minimum of χ^2 over all possible orientations of the torus at each value of L . There is a significant variation in χ^2 as a function of orientation, as noted earlier, and some orientations are strongly preferred over others. In each plot, χ^2 ranges between the uppermost and lowermost solid black curves, as one varies the orientation of the manifold by varying the Euler angles (ϕ, θ, ψ) . For the smallest values of L/L_0 , $\Delta\chi^2$ between the worst and best orientations is 377, 191, and 156 for $\mathcal{M}_{0,1,2}$, respectively. As L/L_0 increases, the effect of a compactified direction decreases. By the time $L/L_0 = 2.6$, the fit results are very close to the case of the infinite manifold \mathbb{R}^3 , and $\Delta\chi^2 \leq 4$ for the different orientations.

We have been unable to find any pattern to the best-fit orientation ϕ, θ, ψ of the torus as a function of L/L_0 . We have examined the possibility that the manifolds we consider are aligned along the axis of evil. To do this, we have chosen the preferred axis of the manifold (the z -axis for \mathbb{T}^3 , the \mathbb{R} direction for $\mathbb{T}^2 \times \mathbb{R}^1$ and the S^1 direction for $S^1 \times \mathbb{R}^2$) to point along the axis-of-evil direction $b = 60^\circ$, $l = -100^\circ$ in galactic coordinates, and allowed for arbitrary rotations of the manifold around this direction. All the angles are varied with step $\pi/100 = 1.8^\circ$. This gives a subset of all the orientations we have considered, and the χ^2 range has been plotted as the dashed colored curves in the figure. The colored curves lie between the black curves (as they must), but they do not lie towards the best-fit χ^2 line. This shows that there is nothing in our computation that picks out the axis-of-evil as a

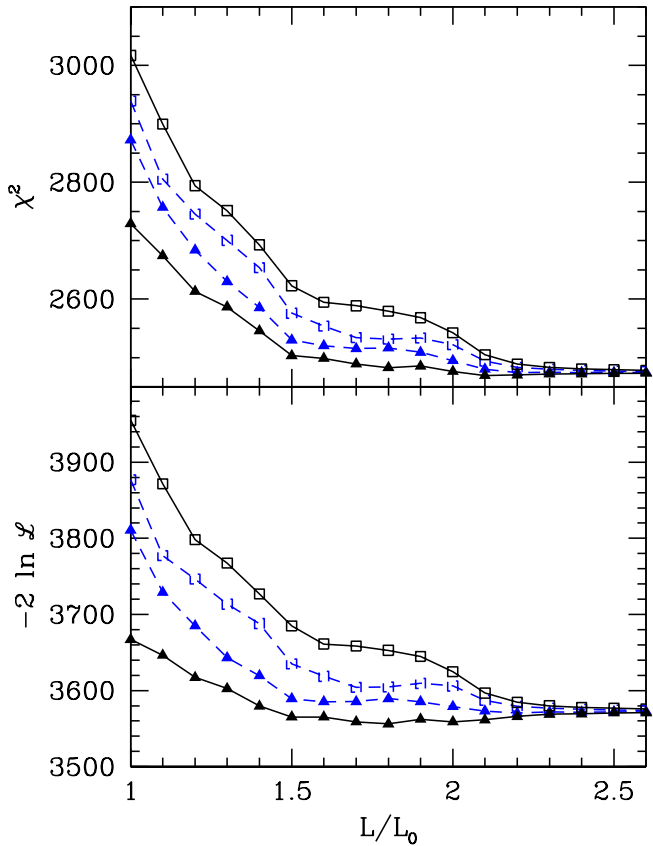


FIG. 5.— Plot of χ^2 and $-2 \ln \mathcal{L}$ against L/L_0 for $\mathcal{M}_0 = \mathbb{T}^3$ for different Euler angles (ϕ, θ, ψ) . The lower solid black curve (solid triangles) is the minimum χ^2 (or $-2 \ln \mathcal{L}$), and the upper solid black curve (open squares) is the maximum χ^2 (or $-2 \ln \mathcal{L}$). The lower dashed colored curve (solid triangles) and upper dashed colored curve (open squares) are the minimum and maximum χ^2 (or $-2 \ln \mathcal{L}$) with a symmetry axis of the manifold restricted to point along the axis of evil.

C.L.	\mathcal{M}_0	\mathcal{M}_1	\mathcal{M}_2
68%	1.47	1.24	0.92
90%	1.33	1.02	0.61
95%	1.24	0.96	0.56

TABLE 1
LIMITS ON L/L_0 USING THE χ^2 GOODNESS-OF-FIT TEST. VALUES LESS THAN THOSE IN THE TABLE ARE EXCLUDED AT THE CONFIDENCE LEVEL GIVEN IN THE FIRST COLUMN.

preferred direction.

We use a goodness-of-fit test to see whether we can rule out the hypothesis that the universe has topology \mathcal{M}_i of size L . The minimum χ^2 values are $\chi^2 = 2469, 2467, 2472$ at $L/L_0 = 2.1, 2.1, 2.2$ for $\mathcal{M}_{0,1,2}$, respectively. Previous studies have also found an indication of a dip in χ^2 around $L/L_0 \sim 2.1$ (Phillips & Kogut 2006). Using the computed values of χ^2 we have the limits given in Table 1.

We estimate confidence intervals for L/L_0 using likelihood ratios (Cash 1979; Eadie et al. 1971)(Nakamura et al. 2010, §33). Maximum likelihood confidence intervals are exact if the distribution is Gaussian. For non-Gaussian distributions, they have an error of order $1/\sqrt{n}$, where n is the number of data

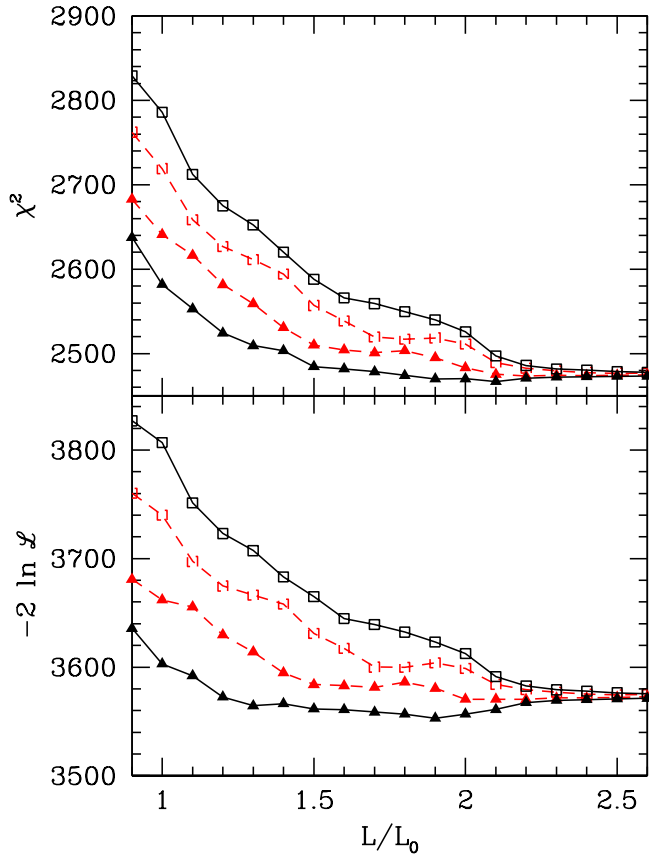


FIG. 6.— Plot of χ^2 and $-2 \ln \mathcal{L}$ against L/L_0 for $\mathcal{M}_1 = \mathbb{T}^2 \times \mathbb{R}^1$ for different Euler angles (ϕ, θ, ψ) . See the Fig. 5 caption.

points (Wilks 1938). The maximum likelihood value is at $L/L_0 = 1.8, 1.9, 1.9$ for $\mathcal{M}_{0,1,2}$, respectively. The confidence intervals for L/L_0 are determined by using $\Delta \ln \mathcal{L}$, the difference of $\ln \mathcal{L}$ from the value that maximizes the likelihood function (Cash 1979; Eadie et al. 1971). Plots of the L/L_0 confidence intervals as a function of $1 - \alpha$, where α is the confidence level, are shown in Figs. 8, 9, 10. The data shows a preference for a finite universe with size $L/L_0 \sim 1.9$ corresponding to $L \sim 27$ Gpc. The allowed L range extends to $L/L_0 \geq 2.6$ at a confidence level $\alpha = 10^{-4}$ for \mathcal{M}_0 , 2×10^{-5} for \mathcal{M}_1 and 4×10^{-3} for \mathcal{M}_2 . Thus the data show evidence for a finite universe at a confidence level $\alpha = 2 \times 10^{-5}$ for the $\mathbb{T}^2 \times \mathbb{R}^1$ topology. The 95% confidence intervals are $L/L_0 \in [1.7, 2.1], [1.8, 2.0], [1.2, 2.1]$ for $\mathcal{M}_{0,1,2}$, respectively.

We have scanned over ~ 4000 different orientations for each value of L , with a finer scan near the minima, so that the error in χ^2 and $-2 \ln \mathcal{L}$ is ≤ 0.5 . The difference in $-2 \ln \mathcal{L}$ between its value at $L \rightarrow \infty$ and its minimum value (which occurs at $L/L_0 = 1.9$ for \mathcal{M}_1) is 20.4, which is well outside possible numerical errors. Note that the main numerical uncertainty is finding the true minimum of $-2 \ln \mathcal{L}$ for finite values of L . The minimum value of $-2 \ln \mathcal{L}$ has been determined with an accuracy ≤ 0.5 . The actual difference in likelihoods between finite and infinite L can only be greater than what we have found. There is an indication that a finite universe fits the data better than an infinite one. However, the “standard” 5 σ -criterion for a discovery, corresponding to a confidence

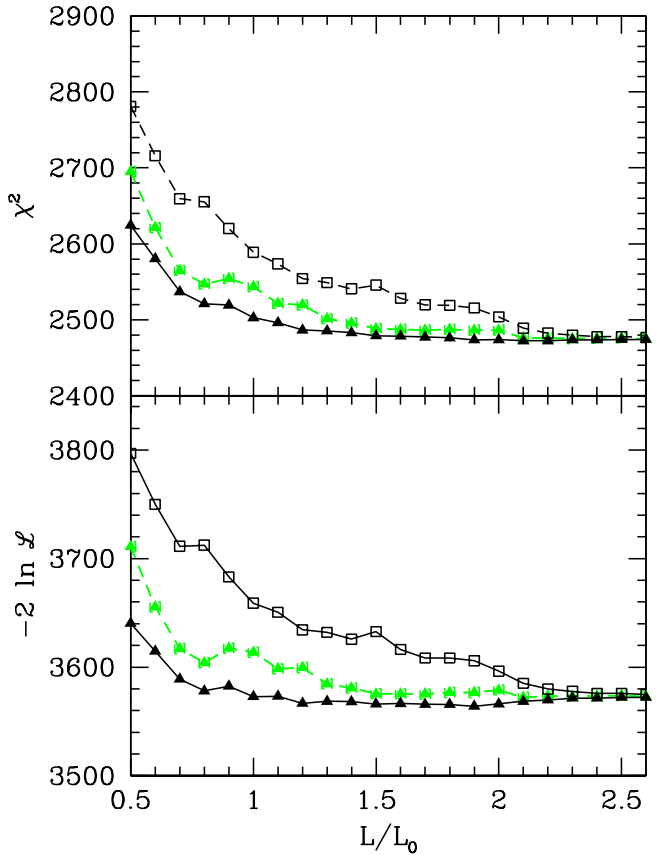


FIG. 7.— Plot of χ^2 and $-2 \ln \mathcal{L}$ against L/L_0 for $\mathcal{M}_2 = S^1 \times \mathbb{R}^2$ for different Euler angles (ϕ, θ, ψ) . The two colored curves are almost on top of each other. See the Fig. 5 caption.

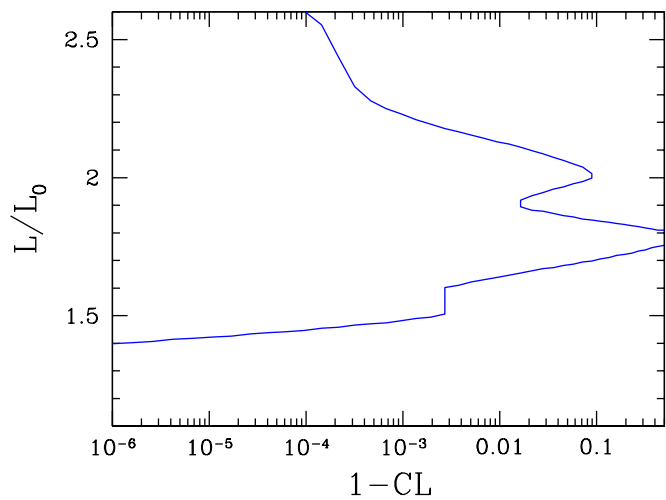


FIG. 8.— Plot of the L/L_0 confidence interval as a function of the confidence level for \mathbb{T}^3 .

level $\alpha = 5.7 \times 10^{-7}$, includes the value $L = \infty$.

The Euler angles for the best fit case \mathcal{M}_1 with $L/L_0 = 1.9$ are $(\phi = 21^\circ \pm 2^\circ, \theta = 53^\circ \pm 2^\circ, \psi = 61^\circ \pm 2^\circ)$ which corresponds, for the infinite direction, to $(b = 37^\circ \pm 2^\circ, l = 291^\circ \pm 2^\circ)$ in galactic coordinates and $(\alpha = 182^\circ \pm 2^\circ, \delta = -25^\circ \pm 2^\circ)$ in J2000 equatorial coordinates. This is close to the direction $(b = 30^\circ \pm 2^\circ, l = 276^\circ \pm 3^\circ)$ of the velocity of the Local Group inferred from the CMB

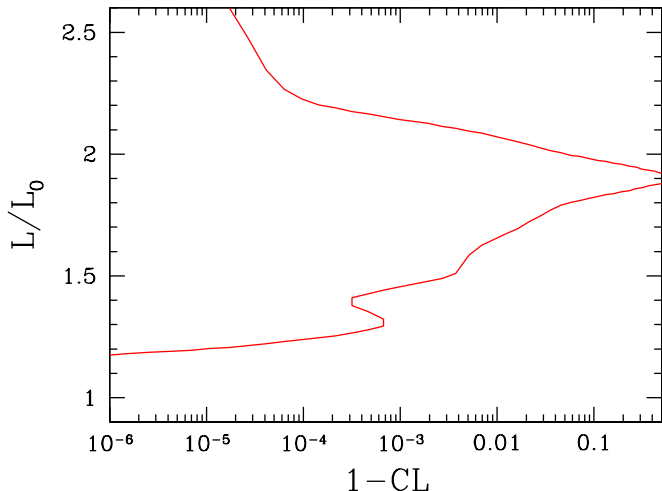


FIG. 9.— Plot of the L/L_0 confidence interval as a function of the confidence level for $\mathbb{T}^2 \times \mathbb{R}^1$.

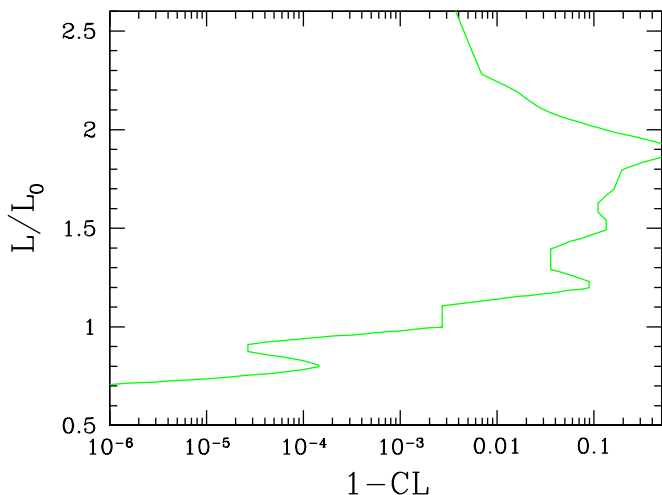


FIG. 10.— Plot of the L/L_0 confidence interval as a function of the confidence level for $S^1 \times \mathbb{R}^2$.

dipole (Lineweaver 1996). We discuss the possibility that our signal is due to a dipole contamination in Sec. 8.

We can compare the probabilities that the universe has topology $\mathcal{M}_{0,1,2,3}$. We use the Bayesian prior that there are four discrete choices, \mathcal{M}_0 with $L/L_0 = 1.8$, \mathcal{M}_1 with $L/L_0 = 1.9$, \mathcal{M}_2 with $L/L_0 = 1.9$, or the infinite case \mathcal{M}_∞ , each of which is equally probable. Since we are comparing four discrete cases, there is no ambiguity due to choice of measure in choosing an equiprobable prior. Then using the likelihood ratios gives the posterior probabilities

$$\begin{aligned} p(\mathcal{M}_0) &= 0.04, \\ p(\mathcal{M}_1) &= 0.96, \\ p(\mathcal{M}_2) &= 2 \times 10^{-5}, \\ p(\mathcal{M}_\infty) &= 1.3 \times 10^{-9}. \end{aligned}$$

The probability of the infinite universe \mathcal{M}_∞ is very small, and the most probable topology is $\mathcal{M}_1 = \mathbb{T}^2 \times \mathbb{R}^1$, with two dimensions compactified, and one infinite.

5.1. Fisher Information

The Fisher information can be used to compute the variance V of the length L determined using the maximum likelihood method. The Fisher information is given by

$$\begin{aligned} V^{-1} &= \frac{1}{2} \left\langle \left(\frac{\partial h}{\partial L} \right)^2 \right\rangle = \text{Tr} C \frac{\partial C^{-1}}{\partial L} C \frac{\partial C^{-1}}{\partial L} \\ &= \text{Tr} C^{-1} \frac{\partial C}{\partial L} C^{-1} \frac{\partial C}{\partial L}. \end{aligned} \quad (42)$$

Using the covariance matrix C for the \mathcal{M}_1 topology with $L/L_0 = 1.9$ gives

$$V^{-1} = 3.3 \times 10^3 \quad (43)$$

so that the error estimate for L/L_0 is $\sqrt{V} = 0.017$. The Fisher information error Eq. (43) corresponds to using a quadratic approximation to the likelihood function about its minimum to determine the error, and gives a smaller error than that obtained earlier using the exact likelihood function.

6. CHECKS

We have been unable to find a simple explanation for the better fit due to a finite topology. However, there are some possibilities which we can test.

The measured cosmic microwave background anisotropy has a smaller value for the quadrupole power C_2 than the theoretical expectation value. There is a large cosmic variance in C_2 , so this is not a discrepancy between theory and experiment. Fig. 2 shows that the predicted value of C_2 for a finite universe is reduced from the infinite universe value. The greater likelihood for a finite universe is not due to lowering the value of C_2 . We have checked this by determining the likelihood using $M_{lm'l'm'}$ for the finite case, but with the $l = l' = 2$ values replaced by their values for the infinite universe. For \mathcal{M}_1 with $L/L_0 = 1.9$, $-2 \ln \mathcal{L}$ increases by 0.43, which is much less than the 20.4 difference in $-2 \ln \mathcal{L}$ from the infinite universe.

As another test, we have computed the likelihood for the \mathcal{M}_1 topology for $L/L_0 = 1.9$ by using a truncated $M_{lm'l'm'}$ matrix. The truncated matrix is constructed by using $M_{lm'l'm'}$ for the finite topology for $5 \leq l, l' \leq 20$, and using $M_{lm'l'm'}$ for the infinite universe, i.e. $M_{lm'l'm'} = C_l \delta_{ll'} \delta_{mm'}$, for l and or l' outside this range. A plot of the likelihood as a function of the Euler angle ψ for this truncated $M_{lm'l'm'}$ is plotted as the dashed blue curve in Fig. 11. This can be compared with the likelihood curve using the full $M_{lm'l'm'}$ for the finite topology, shown as the solid red curve. The dip in the likelihood difference to -20.4 is the signal that the finite topology is a better fit than the infinite universe. The plot for the truncated matrix is similar to that for the full matrix, except that the small-angle fluctuations have been smoothed out, as is to be expected since higher l terms have been dropped. Note that the dip in $2 \ln \mathcal{L}_\infty - 2 \ln \mathcal{L}$ is very similar in both cases, and the minimum of $2 \ln \mathcal{L}_\infty - 2 \ln \mathcal{L}$ is nearly the same. This shows that the effect we find is not due to the low- l modes (quadrupole, octupole), and is also not an edge effect as a result of only using $l \leq 30$ in the computation. For $5 \leq l, l' \leq 20$, $M_{lm'l'm'}$ has 86736

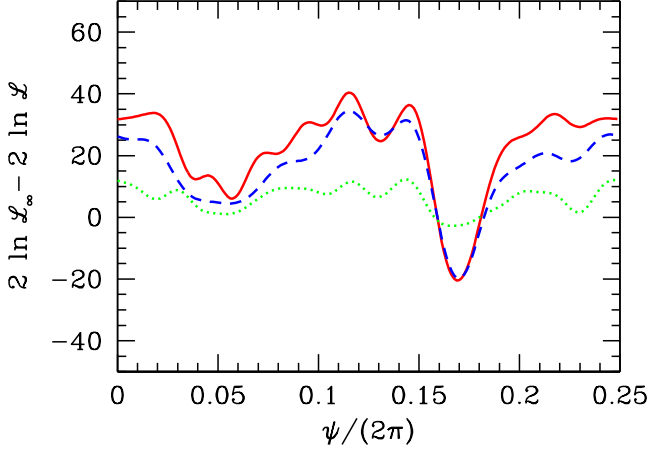


FIG. 11.— Plot of $2 \ln \mathcal{L}_\infty - 2 \ln \mathcal{L}$ against the Euler angle ψ for fixed ϕ, θ for the \mathcal{M}_1 topology for $L/L_0 = 1.9$. The solid red curve uses the full matrix $M_{lm'l'm'}$, the dashed blue curve uses the matrix truncated to $5 \leq l, l' \leq 20$, and the dotted green curve uses the matrix $M_{lm'l'm'} \delta_{ll'}$, retaining only the part diagonal in l .

elements of which 11056 satisfy the $l \equiv l' \pmod{2}$, $m \equiv m' \pmod{4}$ condition and are non-zero.

The off-diagonal elements in $M_{lm'l'm'}$ are important for the calculations. We have also computed the likelihood by retaining only the elements which are diagonal in l , i.e. using $M_{lm'l'm'} \delta_{ll'}$. This drops the elements in $M_{lm'l'm'} \delta_{ll'}$ which are off-diagonal in l , while retaining the elements which are off-diagonal in m for a given l . The likelihood with this matrix is the dashed green curve in Fig. 11. With this matrix, the likelihood deviates much less from the infinite universe, and the dip near $\psi/(2\pi) \approx 0.17$ is much less pronounced.

7. MONTE-CARLO SKIES

The results of the previous section were obtained using a likelihood analysis of the WMAP7 data. One can study whether the better fit of a finite topology is due to a statistical fluctuation. Since the big-bang is not a repeatable experiment, this must be done by generating random Monte-Carlo data for the pixels Δ_i , and redoing the analysis for this Monte-Carlo data. To actually do this numerically is beyond the computing power we have available. Luckily, for the problem at hand, we can analyze the Monte-Carlo problem analytically.

Assume that the pixels Δ_i are generated by the covariance matrix C_∞ for an infinite universe, so that the probability distribution is

$$p(\Delta) = \frac{1}{\sqrt{\det(2\pi C_\infty)}} \exp\left(-\frac{1}{2} \Delta^T C_\infty^{-1} \Delta\right). \quad (44)$$

The likelihood function computed using Δ_i and covariance matrix C (of a finite universe) is

$$-2 \log \mathcal{L} = \Delta^T C^{-1} \Delta + \ln \det(2\pi C), \quad (45)$$

and the likelihood constructed using the covariance matrix C_∞ of the infinite universe is

$$-2 \log \mathcal{L}_\infty = \Delta^T C_\infty^{-1} \Delta + \ln \det(2\pi C_\infty). \quad (46)$$

Let

$$h \equiv (-2 \log \mathcal{L}_\infty) - (-2 \log \mathcal{L}), \quad (47)$$

be the difference of the two log-likelihoods. In our analysis, we found $h = 20.4 > 0$, so that the finite universe was more likely than the infinite universe. The average value of h over Monte-Carlo data can be computed using Eq. (44) and Eq. (47). The two-point function is

$$\langle \Delta_i \Delta_j \rangle = (C_\infty)_{ij}, \quad (48)$$

so that

$$\langle h \rangle = N - \text{Tr } C^{-1} C_\infty + \ln \det(C_\infty) - \ln \det(C). \quad (49)$$

It is convenient to define the symmetric matrix

$$S = C_\infty^{1/2} C^{-1} C_\infty^{1/2}, \quad (50)$$

which is a positive matrix since C and C_∞ are positive matrices, and has eigenvalues $s_i > 0$. In terms of S ,

$$\begin{aligned} \langle h \rangle &= N - \text{Tr } S + \ln \det S \\ &= \sum_i [1 - s_i + \ln s_i]. \end{aligned} \quad (51)$$

The function $1 - s + \ln s \leq 0$ with its maximum at 0 when $s = 1$. Thus

$$\langle h \rangle \leq 0 \quad (52)$$

and $\langle h \rangle = 0$ only if $S = \mathbf{1}$, i.e. $C = C_\infty$. This gives the intuitively obvious result that the best fit for data generated with covariance matrix C_∞ is, on average, given by fitting using the same covariance matrix C_∞ . Any other covariance matrix C used for fitting, on average, gives a lower likelihood.

If instead of Eq. (47) we had used the difference of χ^2 ,

$$h_\chi \equiv \chi_\infty^2 - \chi^2, \quad (53)$$

then

$$\langle h_\chi \rangle = N - \text{Tr } C^{-1} C_\infty = N - \text{Tr } S = \sum_i [1 - s_i], \quad (54)$$

and $\langle h_\chi \rangle$ could have either sign, since $s_i > 0$, but need not be smaller than 1. For example, a simple rescaling, $C = \lambda C_\infty$, with $\lambda \rightarrow \infty$ can always make $\chi^2 \rightarrow 0$, its minimum possible value. This option is eliminated for likelihood because of the $\det(2\pi C)$ term.

Using for C the best-fit topology \mathcal{M}_1 with $L/L_0 = 1.9$, we find the numerical values

$$\begin{aligned} N &= 2482, \\ \ln \det(C_\infty) &= 1097.8 + \ln \det C_f, \\ \ln \det(C) &= 1082.73 + \ln \det C_f, \\ \text{Tr } C^{-1} C_\infty &= \text{Tr } S = 2516.6, \end{aligned} \quad (55)$$

so that

$$\langle h \rangle = -19.5. \quad (56)$$

This differs from the value we find of $h = +20.9$ by $\Delta h = h - \langle h \rangle = 40.4$. The probability that Δh is a statistical fluctuation can be determined by computing the variance of h using the four-point function

$$\begin{aligned} \langle \Delta_i \Delta_j \Delta_k \Delta_l \rangle &= (C_\infty)_{ij} (C_\infty)_{kl} + (C_\infty)_{ik} (C_\infty)_{jl} \\ &\quad + (C_\infty)_{il} (C_\infty)_{jk}, \end{aligned} \quad (57)$$

to obtain

$$\begin{aligned} \langle (\Delta h)^2 \rangle &= 2N + 2\text{Tr} C^{-1} C_\infty C^{-1} C_\infty - 4 (\text{Tr} C^{-1} C_\infty) \\ &= 2\text{Tr} (1 - C^{-1} C_\infty)^2 = 2\text{Tr} (1 - S)^2. \end{aligned} \quad (58)$$

In our case,

$$\text{Tr} C^{-1} C_\infty C^{-1} C_\infty = 2610.0, \quad (59)$$

so that

$$\langle (\Delta h)^2 \rangle = 117.6 = (10.8)^2. \quad (60)$$

Our observed value of $\Delta h = 40.4$ is 3.7σ away from the mean, so the probability that a fluctuation gives h larger than or equal to our observed value is 1.1×10^{-4} , assuming a normal distribution.

While the distribution of the data Δ_i is Gaussian, the distribution of the likelihood difference h is no longer Gaussian. We can also compute higher order connected correlation functions of h ,

$$\begin{aligned} \langle (\Delta h)^r \rangle_c &= 2^r (r-1)! \text{Tr} (1 - C^{-1} C_\infty)^r \\ &= 2^r (r-1)! \text{Tr} (1 - S)^r, \end{aligned} \quad (61)$$

from the generating function

$$\begin{aligned} \log \langle e^{\lambda \Delta h} \rangle &= -\lambda \text{Tr} (1 - C^{-1} C_\infty) \\ &\quad - \frac{1}{2} \text{Tr} \ln [1 - 2\lambda(1 - C^{-1} C_\infty)] \\ &= -\lambda \text{Tr} (1 - S) - \frac{1}{2} \text{Tr} \ln [1 - 2\lambda(1 - S)], \end{aligned} \quad (62)$$

so that

$$\begin{aligned} \langle (\Delta h)^3 \rangle &= 8 \text{Tr} (1 - C^{-1} C_\infty)^3 \\ \langle (\Delta h)^4 \rangle_c &= 48 \text{Tr} (1 - C^{-1} C_\infty)^4, \end{aligned} \quad (63)$$

where the fourth-order correlation is

$$\langle (\Delta h)^4 \rangle = \langle (\Delta h)^4 \rangle_c + 3 \langle (\Delta h)^2 \rangle^2, \quad (64)$$

in terms of the connected correlation. The mean value $\langle h \rangle$, and all the connected correlation functions $\langle (\Delta h)^r \rangle_c$ are of order N , the number of data points. Thus the relative correlation $\langle (\Delta h)^r \rangle / \langle h \rangle^r$ is of order N^{1-r} .

The numerical values for our case are

$$\begin{aligned} \langle (\Delta h)^3 \rangle &= -489.0, \\ \langle (\Delta h)^4 \rangle_c &= 4303.7. \end{aligned} \quad (65)$$

We can get a better estimate of the probability that $h = 20.4$ is due to a statistical fluctuation by using these higher order moments. We have fit $\langle h \rangle$ and $\langle (\Delta h)^r \rangle$, $r = 2, 3, 4$ to a probability distribution

$$\begin{aligned} p(h) &= p_0 \exp[-(h - h_0)^2 - c_2(h - h_0)^2 \\ &\quad - c_3(h - h_0)^3 - c_4(h - h_0)^4], \end{aligned} \quad (66)$$

and found using this distribution that the probability that $h - \langle h \rangle \geq 40.4$ is 10^{-6} , which is smaller than the value obtained earlier using a normal distribution for h .

8. DIPOLE CONTAMINATION

The symmetry axis of \mathcal{M}_1 points in the direction ($b = 37^\circ \pm 2^\circ, l = 291^\circ \pm 2^\circ$), which is close to the direction of the velocity of the Local Group ($b = 30^\circ \pm 2^\circ, l = 276^\circ \pm 3^\circ$) (Lineweaver 1996). The CMB has a large dipole asymmetry of $3.358 \pm 0.001 \pm 0.023$ mK in the direction ($b = 48.05^\circ \pm 0.11^\circ, l = 264.31^\circ \pm 0.2^\circ$) (Lineweaver 1996). Suppose that the data is contaminated by a dipole contribution that has not been properly subtracted out.³ Could a residual dipole explain the results we have found?

To study the effect of a residual dipole, assume that the observed pixels are

$$\Delta_i^{\text{obs}} = \Delta_i + \mathbf{p} \cdot \hat{\mathbf{n}}_i = \Delta_i + d_i, \quad d_i = \mathbf{p} \cdot \hat{\mathbf{n}}_i \quad (67)$$

where Δ_i are the true fluctuations given by the distribution Eq. (44) and \mathbf{p} is the residual dipole contamination in the data. Then Eq. (45,46) are replaced by

$$\begin{aligned} -2 \log \mathcal{L} &= (\Delta + d)^T C_i^{-1} (\Delta + d) + \ln \det(2\pi C), \\ -2 \log \mathcal{L}_i &= (\Delta + d)^T C_i^{-1} (\Delta + d) + \ln \det(2\pi C). \end{aligned} \quad (68)$$

From these, we find

$$\begin{aligned} \langle h \rangle &= N - \text{Tr} C^{-1} C_\infty + \ln \det(C_\infty) - \ln \det(C) \\ &\quad + (d^T C_\infty^{-1} d) - (d^T C^{-1} d), \\ \langle \Delta h^2 \rangle &= 2N - 8d^T C^{-1} d + 4d^T C_\infty^{-1} d + 4d^T C^{-1} C_\infty C^{-1} d \\ &\quad + 2\text{Tr} C^{-1} C_\infty C^{-1} C_\infty - 4 (\text{Tr} C^{-1} C_\infty). \end{aligned} \quad (69)$$

Dipole contamination produces a systematic shift in h from its value in Eq. (49) given by the $(d^T C_\infty^{-1} d) - (d^T C^{-1} d)$ terms, which can be written as

$$(d^T C_\infty^{-1} d) - (d^T C^{-1} d) = p_\alpha p_\beta D_{\alpha\beta} \quad (70)$$

in term of the components $p_\alpha = (p_x, p_y, p_z)$ of the dipole. We find

$$D = \begin{bmatrix} -1.22 & -0.004 & -0.114 \\ -0.004 & -0.0281 & -0.003 \\ -0.114 & -0.003 & -0.0127 \end{bmatrix} \text{mK}^{-2} \quad (71)$$

The largest eigenvalue is -1.23mK^{-2} . To get a shift in $-2 \ln \mathcal{L}$ of 20.4 requires a dipole contamination $|\mathbf{p}|$ of around 4mK^{-2} . This is larger than the observed dipole, and several hundred times the quoted uncertainty in the CMB dipole (Lineweaver 1996), and is excluded.

9. CONCLUSIONS

We have analyzed the possibility that the universe has compact topologies $\mathcal{M}_0 = \mathbb{T}^3$, $\mathcal{M}_1 = \mathbb{T}^2 \times \mathbb{R}^1$ and $\mathcal{M}_2 = S^1 \times \mathbb{R}^2$ using modifications of the available CAMB and WMAP 7-year likelihood codes. The maximum likelihood 95% confidence intervals are $1.7 \leq L/L_0 \leq 2.1$, $1.8 \leq L/L_0 \leq 2.0$, $1.2 \leq L/L_0 \leq 2.1$ for the three cases, respectively. Using the Bayesian analysis discussed earlier, we find that the most probable universe has the compact topology \mathcal{M}_1 . An infinite universe is compatible with the data at a confidence level of 2×10^{-5} (i.e. 4.3σ). We find no evidence of a preference for the axis-of-evil direction. The improved fit for a finite universe

³ This possibility was suggested to us by B. Keating.

is not due to the lowered prediction for the quadrupole anisotropy; this accounts for only a small fraction of the increase in likelihood.

It would be useful to investigate whether any systematic effects in the WMAP data introduce effects with cubic symmetry that can mimic the effects of a torus topology. The best fit results do not pick out any special orientation for the torus, such as a torus with symmetry axis perpendicular to the galactic plane, that might lead to systematic effects that lead to a fake signal. Pixelization of the data using the HEALPix grid also should not introduce cubic symmetry terms along an axis not aligned with the galactic pole. The best fit results for

\mathcal{M}_1 have symmetry axis which is near ($\sim 10^\circ$) the direction of the Local Group velocity.

We would like to thank K. Griest, B. Keating, and A. Wolfe for helpful discussions and for comments on the manuscript. We thank Terrence Martin and Frank Wuerthwein for showing us how to use the DOE OSG cluster, the LAMBDA team for making the seven-year WMAP data and the likelihood calculation software available online, and Antony Lewis and Anthony Challinor for making the CAMB software available online.

REFERENCES

- Arnowitt, R. L., Deser, S., & Misner, C. W. 2008, *General Relativity and Gravitation*, 40, 1997, gr-qc/0405109
- Aurich, R. 2008, *Class. Quant. Grav.*, 25, 225017, 0803.2130
- Aurich, R., Janzer, H. S., Lustig, S., & Steiner, F. 2008, *Class. Quant. Grav.*, 25, 125006, 0708.1420
- Aurich, R., & Lustig, S. 2010, 1009.5880
- Aurich, R., Lustig, S., & Steiner, F. 2005a, *Class. Quant. Grav.*, 22, 3443, astro-ph/0504656
- . 2005b, *Class. Quant. Grav.*, 22, 2061, astro-ph/0412569
- . 2006, *Mon. Not. Roy. Astron. Soc.*, 369, 240, astro-ph/0510847
- Aurich, R., Lustig, S., Steiner, F., & Then, H. 2004, *Class. Quant. Grav.*, 21, 4901, astro-ph/0403597
- . 2005c, *Phys. Rev. Lett.*, 94, 021301, astro-ph/0412407
- Barrow, J. D., & Kodama, H. 2001, *Int. J. Mod. Phys.*, D10, 785, gr-qc/0105049
- Bennett, C. L., et al. 1996, *Astrophys. J.*, 464, L1, astro-ph/9601067
- Bielewicz, P., & Banday, A. J. 2011, *MNRAS*, 137, 1012.3549
- Bielewicz, P., & Riazuelo, A. 2008, 0804.2437
- Blancoil, V., & Roukema, B. F. 2000, astro-ph/0010170
- Bond, J. R., Pogosian, D., & Souradeep, T. 2000, *Phys. Rev.*, D62, 043005, astro-ph/9912124
- Caillerie, S., et al. 2007, *Astron. Astrophys.*, 476, 691, 0705.0217
- Cash, W. 1979, *Astrophys. J.*, 228, 939
- Cornish, N. J., Spergel, D. N., & Starkman, G. D. 1998, *Class. Quant. Grav.*, 15, 2657, astro-ph/9801212
- Cornish, N. J., Spergel, D. N., Starkman, G. D., & Komatsu, E. 2004, *Phys. Rev. Lett.*, 92, 201302, astro-ph/0310233
- Cresswell, J. G., Liddle, A. R., Mukherjee, P., & Riazuelo, A. 2006, *Phys. Rev.*, D73, 041302, astro-ph/0512017
- de Oliveira-Costa, A., Smoot, G. F., & Starobinsky, A. A. 1996, *Astrophys. J.*, 468, 457, astro-ph/9510109
- de Oliveira Costa, A., & Smoot, G. F. 1995, *Astrophys. J.*, 448, 477, astro-ph/9412003
- de Sitter, W. 1917, *Proc. Roy. Acad. Amsterdam*, 20, 229
- Dineen, P., Rocha, G., & Coles, P. 2005, *Mon. Not. Roy. Astron. Soc.*, 358, 1285, astro-ph/0404356
- Dodelson, S. 2003, *Modern Cosmology* (Academic Press)
- Eadie, W., Drijard, D., James, F., Roos, M., & Sadoulet, B. 1971, *Statistical Methods in Experimental Physics* (North Holland, Amsterdam)
- Friedmann, A. 1924, *Zeitschrift für Physik A Hadrons and Nuclei*, 21, 326, 10.1007/BF01328280
- Gomero, G. I. 2002, *Int. J. Mod. Phys.*, A17, 4281, astro-ph/0210279
- . 2003, *Class. Quant. Grav.*, 20, 4775, astro-ph/0305071
- Gomero, G. I., Reboucas, M. J., & Tavakol, R. 2002a, *Int. J. Mod. Phys.*, A17, 4261, gr-qc/0210016
- Gomero, G. I., Reboucas, M. J., & Teixeira, A. F. F. 2000, *Int. J. Mod. Phys.*, D9, 687, gr-qc/0105048
- . 2001, *Class. Quant. Grav.*, 18, 1885, gr-qc/9911049
- Gomero, G. I., Teixeira, A. F. F., Reboucas, M. J., & Bernui, A. 2002b, *Int. J. Mod. Phys.*, D11, 869, gr-qc/9811038
- Gorski, K., Hivon, E., Banday, A., Wandelt, B., Hansen, F., et al. 2005, *Astrophys. J.*, 622, 759, astro-ph/0409513
- Gundermann, J. 2005, astro-ph/0503014
- Hajian, A., & Souradeep, T. 2003, astro-ph/0301590
- Hipolito-Ricaldi, W. S., & Gomero, G. I. 2005, *Phys. Rev.*, D72, 103008, astro-ph/0507238
- Jarosik, N., et al. 2011, *Astrophys. J. Suppl.*, 192, 14, 1001.4744
- Komatsu, E., et al. 2011, *Astrophys. J. Suppl.*, 192, 18, 1001.4538
- Kunz, M., et al. 2006, *Phys. Rev.*, D73, 023511, astro-ph/0510164
- Lachieze-Rey, M., & Luminet, J.-P. 1995, *Phys. Rept.*, 254, 135, gr-qc/9605010
- Land, K., & Magueijo, J. 2005, *Phys. Rev. Lett.*, 95, 071301, astro-ph/0502237
- . 2007, *Mon. Not. Roy. Astron. Soc.*, 378, 153, astro-ph/0611518
- Larson, D., et al. 2011, *Astrophys. J. Suppl.*, 192, 16, 1001.4635
- Levin, J. 2004a, *Phys. Rev. D*, 70, 083001
- Levin, J. J. 2002, *Phys. Rept.*, 365, 251, gr-qc/0108043
- . 2004b, astro-ph/0403036
- Lew, B. S., & Roukema, B. F. 2008, *Astron. Astrophys.*, 482, 747, 0801.1358
- Lewis, A., Challinor, A., & Lasenby, A. 2000, *Astrophys. J.*, 538, 473, astro-ph/9911177
- Linde, A. D. 2004, *JCAP*, 0410, 004, hep-th/0408164
- Lineweaver, C. H. 1996, astro-ph/9609034
- Luminet, J.-P. 2008, 0802.2236
- Luminet, J. P., Weeks, J., Riazuelo, A., Lehoucq, R., & Uzan, J. P. 2003, *Nature*, 425, 593, astro-ph/0310253
- Marecki, A., Roukema, B. F., & Bajtlik, S. 2005, *Astron. Astrophys.*, 435, 427, astro-ph/0412181
- Menzies, D., & Mathews, G. J. 2005, *JCAP*, 0510, 008, astro-ph/0503555
- Mota, B., Reboucas, M. J., & Tavakol, R. 2005, *Int. J. Mod. Phys.*, A20, 2415, astro-ph/0503683
- . 2008, *Phys. Rev.*, D78, 083521, 0808.1572
- . 2010, *Phys. Rev.*, D81, 103516, 1002.0834
- Nakamura, K., et al. 2010, *J.Phys.G*, G37, 075021
- Niarhou, A., & Jaffe, A. 2007, *Phys. Rev. Lett.*, 99, 081302, astro-ph/0702436
- Opher, R. 2004, astro-ph/0408142
- Phillips, N. G., & Kogut, A. 2006, *Astrophys. J.*, 645, 820, astro-ph/0404400
- Planck Collaboration. 2006, astro-ph/0604069
- Rakic, A., & Schwarz, D. J. 2007, *Phys. Rev.*, D75, 103002, astro-ph/0703266
- Reboucas, M. J. 2000, *Int. J. Mod. Phys.*, D9, 561, gr-qc/0007040
- Reboucas, M. J., & Gomero, G. I. 2004, *Braz. J. Phys.*, 34, 1358, astro-ph/0402324
- Riazuelo, A., Weeks, J., Uzan, J.-P., Lehoucq, R., & Luminet, J.-P. 2004, *Phys. Rev.*, D69, 103518, astro-ph/0311314
- Roukema, B. F. 2000, *Bull. Astron. Soc. India*, 28, 483, astro-ph/0010185
- . 2005, *Astron. Astrophys.*, 439, 479, astro-ph/0409694
- . 2009, *Int. J. Mod. Phys.*, D18, 2237, 0905.2543
- . 2010, 1002.3528
- Roukema, B. F., & Blancoil, V. 2010, *Class. Quant. Grav.*, 27, 245001, 0912.2300
- Roukema, B. F., Bulinski, Z., Szaniewska, A., & Gaudin, N. E. 2008, *Astron. Astrophys.*, 486, 55, 0801.0006
- Roukema, B. F., Lew, B., Cechowska, M., Marecki, A., & Bajtlik, S. 2004, *Astron. Astrophys.*, 423, 821, astro-ph/0402608
- Schwartzschild, K. 1900, *Vierteljahrsschrift der Ast. Ges.*, 35, 337
- Seljak, U., & Zaldarriaga, M. 1996, *Astrophys. J.*, 469, 437, astro-ph/9603033
- Shapiro Key, J., Cornish, N. J., Spergel, D. N., & Starkman, G. D. 2007, *Phys. Rev.*, D75, 084034, astro-ph/0604616
- Sokolov, I. Y. 1993, *JETP Lett.*, 57, 617
- Starkman, G. D. 1998, *Class. Quant. Grav.*, 15, 2529
- Starobinsky, A. A. 1993, *JETP Lett.*, 57, 622, gr-qc/9305019
- Stevens, D., Scott, D., & Silk, J. 1993, *Phys. Rev. Lett.*, 71, 20
- Stewart, J. M., Stewart, M. E., & Schwarzschild, K. 1998, *Class. Quant. Grav.*, 15, 2539
- Weeks, J., Luminet, J.-P., Riazuelo, A., & Lehoucq, R. 2004, *Mon. Not. Roy. Astron. Soc.*, 352, 258, astro-ph/0312312
- Wilks, S. 1938, *Ann. Math. Stat.*, 9, 60
- Zeldovich, Y. B., & Starobinsky, A. A. 1984, *Sov. Astron. Lett.*, 10, 135